

DISCOVERY OF A TIME LAG BETWEEN THE SOFT X-RAY AND RADIO EMISSION OF THE TIDAL DISRUPTION FLARE ASASSN-14LI: EVIDENCE FOR LINEAR DISK–JET COUPLING

DHEERAJ R. PASHAM¹

Massachusetts Institute of Technology, Cambridge, MA, 02139

AND

SJOERT VAN VELZEN²

Johns Hopkins University, Department of Physics & Astronomy, Baltimore, MD 21218

Draft version February 22, 2019

ABSTRACT

The tidal disruption of a star by a supermassive black hole can result in transient radio emission. The electrons producing these synchrotron radio flares could either be accelerated inside a relativistic jet or externally by shocks resulting from an outflow interacting with the circumnuclear medium. Until now, evidence for the internal emission mechanism has been lacking; nearly all tidal disruption flare studies have adopted the external shock model to explain the observed properties of radio flares. Here we report a result that presents a challenge to external emission models: we discovered a cross-correlation between the soft X-ray (0.3-1 keV) and 16 GHz radio flux of the tidal disruption flare ASASSN-14li. Variability features in the X-ray light curve appear again in the radio light curve, but after a time lag of about 13 days. This demonstrates that soft X-ray emitting accretion disk regulates the radio emission. This coupling appears to be inconsistent with all previous external emission models for this source but is naturally explained if the radio emission originates from a freely expanding jet. We show that emission internal to an adiabatically expanding jet can also reproduce the observed evolution of the radio spectral energy distribution. Furthermore, both the correlation between X-ray and radio luminosity as well as our radio spectral modeling imply an approximately linear coupling between the accretion rate and jet power.

1. INTRODUCTION

The tidal disruption of a star by a massive black hole ($\gtrsim 10^4 M_{\odot}$) can lead to a spectacular flare that is observable across the entire electromagnetic spectrum. Thermal, i.e., blackbody emission, is detected at optical/UV (Gezari et al. 2009; van Velzen et al. 2011; Arcavi et al. 2014) and soft X-ray (Bade et al. 1996; Esquej et al. 2008) frequencies and is thought to originate from the tidal debris of the star (e.g., Pasham et al. 2017). Dust reprocessing of this thermal flare can yield a transient signal at mid-infrared wavelengths (e.g., van Velzen et al. 2016a).

A handful of candidate stellar tidal disruption flares (TDFs) that have been discovered by their thermal emission are also detected at radio frequencies: ASASSN-14li (van Velzen et al. 2016b; Alexander et al. 2016), XMMSL1 J074085 (Saxton et al. 2017; Alexander et al. 2017), and IGR J12580+0134 (Irwin et al. 2015; Perlman et al. 2017)—although the latter is perhaps more likely explained by activity of a pre-existing active galactic nucleus (see Auchettl et al. 2017 for further discussion). The radio luminosities of these sources are $\sim 10^{38}$ erg s⁻¹ and fade with a characteristic time scale of a few months. The equipartition energy of the observed radio emission from ASASSN-14li is $\sim 10^{48}$ erg (Alexander et al. 2016). This rather low energy and short lifetime leaves open the possibility that such low-luminosity radio flares are common for thermal TDFs. Most radio follow-up observations (e.g.,

Bower et al. 2013; van Velzen et al. 2013) were simply not sensitive enough to detect such events—however see Blagorodnova et al. (2017) for a recent counterexample.

The radio luminosity of the thermal TDFs is over three orders of magnitude lower than the radio luminosity of the TDFs that have been discovered by their non-thermal γ -ray emission (Bloom et al. 2011; Zauderer et al. 2011; Levan et al. 2011; Zauderer et al. 2011; Burrows et al. 2011; Cenko et al. 2012; Brown et al. 2015; Pasham et al. 2015). The non-thermal X-ray emission of these TDFs is best-explained by Doppler boosted emission caused by a relativistic jet observed at a small inclination. Synchrotron emission due to electrons accelerated in the forward shock of this jet can explain the observed radio light curves (Giannios & Metzger 2011; Metzger et al. 2012; Berger et al. 2012; Mimica et al. 2015; Generozov et al. 2017). This external emission mechanism is akin to models for radio afterglows of γ -ray bursts (e.g., Piran 2004; Nakar & Piran 2011) or supernovae (Chevalier 1998). The isotropic energy of the jet that powers the non-thermal TDFs is $\sim 10^{53}$ erg (e.g., Mimica et al. 2015).

An external emission model could also explain the observed radio light curves of thermal TDFs. If the accretion onto the black hole exceeds its Eddington limit, we might anticipate the launch of a photon-driven wind (e.g., Sądowski & Narayan 2016). When this wind interacts with the circumnuclear medium, shocks can accelerate electrons to yield synchrotron emission (Alexander et al. 2016, 2017). An alternative scenario has been proposed by Krolik et al. (2016), who suggests that shocks driven by the unbound stellar debris streams

¹ NASA Einstein Fellow; dheeraj@space.mit.edu

² NASA Hubble Fellow; sjoert@jhu.edu

are responsible for producing the synchrotron-emitting electrons. Finally, a third possibility is that the radio emission originates from a forward shock of a relativistic jet that is being decelerated by the circumnuclear medium (van Velzen et al. 2016b).

We are thus presented with a dichotomy of radio power from TDFs (Generozov et al. 2017): low power thermal TDFs and high power non-thermal TDFs. However, since the nature of radio emission of the radio-weak TDFs is debated, interpreting this dichotomy is difficult. If the radio-weak TDFs are also due to a jet, a unified picture emerges in which all tidal disruptions lead to jet launching (van Velzen et al. 2011), and the observed radio power dichotomy translates into a jet power dichotomy. If, on the other hand, radio-weak TDFs are explained by a disk-wind or unbound debris, the observed radio power dichotomy could be explained by the initial conditions that are required for the launch of a relativistic jet (e.g., Tchekhovskoy et al. 2014).

The goal of this work is to carry out a cross-correlation analysis between the X-ray and the radio light curves of ASASSN-14li to understand the nature of the radio emission of this thermal TDF. Below we first briefly introduce this “Rosetta stone” TDF. We then present the details of its radio and X-ray observations in Section 2, followed by the cross-correlation analysis in Section 3. We then discuss our new jet model for the synchrotron emission of this source in Section 4 and close with a discussion in Section 5.

1.1. ASASSN-14li

The optical transient ASASSN-14li was discovered by the All-Sky Automated Survey for SuperNovae (ASASSN; Shappee et al. 2014) on 22 November 2014 (Holoien et al. 2016a). Within a few weeks it became clear that this source displayed nearly all the known properties of previous optical TDFs: an origin consistent with the nucleus of the host galaxy, an optical spectrum with broad Hydrogen and Helium emission lines, and a constant blue optical/UV color, corresponding to a temperature of roughly 3×10^4 K (Holoien et al. 2016a).

Two properties are unique to ASASSN-14li: the detection of a luminous, thermal X-ray flare (Miller et al. 2015) and the detection of a low-luminosity ($\approx 10^{38}$ ergs $^{-1}$ at 16 GHz) radio flare (van Velzen et al. 2016b; Alexander et al. 2016). The size of the X-ray emitting region as inferred from energy spectral modeling and fast time variability is only a few gravitational radii (Miller et al. 2015). This small radius, combined with the fact that the X-ray spectrum is thermal, suggests that the X-rays originate from the innermost regions of the accretion flow (Krolik et al. 2016). Because relativistic ejections—which can produce synchrotron radio emission—are also launched from close to the black hole, ASASSN-14li provides a unique laboratory to understand the connection, if any, between the accretion and the ejection of matter near a black hole.

Thanks to its very low redshift, observations with European VLBI Network (EVN) could spatially resolve the radio emission from ASASSN-14li (Romero-Cañizales et al. 2016). The 5 GHz EVN observations—taken about 200 days after its discovery—revealed a stationary feature with a size of a few mil-

TABLE 1
SUMMARY OF X-RAY SPECTRAL MODELING.

MJD range	N_H (10^{22} cm $^{-2}$)	T (keV)	χ^2/dof
56991-57008	$0.007^{+0.023}_{-0.007}$	$0.058^{+0.003}_{-0.004}$	1.188/30
57011-57030	$0.027^{+0.026}_{-0.023}$	$0.059^{+0.004}_{-0.004}$	1.317/32
57033-57046	$0.023^{+0.021}_{-0.019}$	$0.066^{+0.003}_{-0.003}$	1.235/33
57049-57075	$0.055^{+0.028}_{-0.025}$	$0.054^{+0.004}_{-0.004}$	1.099/30
57078-57121	$0.032^{+0.030}_{-0.026}$	$0.056^{+0.005}_{-0.005}$	0.601/29
57124-57177	$0.018^{+0.033}_{-0.018}$	$0.052^{+0.005}_{-0.005}$	0.848/26
57179-57361	$0.090^{+0.058}_{-0.034}$	$0.041^{+0.004}_{-0.006}$	1.170/25

NOTE. — N_H , and T are the best-fit Hydrogen column and the black body temperature, respectively, of ASASSN-14li’s 0.3-1.0 keV average X-ray spectra. The reduced χ^2 along with the degrees of freedom (dof) for the X-ray spectral fit are shown in the last column.

liarcseconds (mas) and a second component ≈ 2 parsecs away with a factor of 6 lower in flux.

The host galaxy of ASASSN-14li is a post-starburst galaxy—TDFs happen preferentially in these rare types of galaxies (Arcavi et al. 2014; French et al. 2016). Integral field spectroscopic observations of the host revealed ionized filaments, similar to ionization nebulae around fading AGNs (Prieto et al. 2016). Indeed the detection of low-luminosity radio emission prior to the tidal disruption is best-explained by a low-luminosity AGN (Holoien et al. 2016b; van Velzen et al. 2016b; Alexander et al. 2016).

2. RADIO AND X-RAY OBSERVATIONS

2.1. Radio Data

The data used in this work were acquired by four different telescopes. The Arcminute Microkelvin Imager (AMI) and the Westerbork Synthesis Radio Telescope (WSRT) provided 16 GHz and 1.4 GHz radio data, respectively (van Velzen et al. 2016b). Further multi-epoch radio spectral energy distribution (SED) data was acquired by the very large array (VLA) (Alexander et al. 2016). Finally, *Swift*’s (Gehrels et al. 2004) X-Ray Telescope (XRT; Burrows et al. 2005) provided the 0.3-10.0 keV X-ray data.

The pre-flare radio flux of ASASSN-14li, based on archival data, is orders of magnitude higher than what is expected from star formation alone. This indicates that a weak AGN was present prior to the flare (Holoien et al. 2016a; van Velzen et al. 2016b; Alexander et al. 2016). From the plateau in the late-time AMI light curve we infer that the baseline (i.e., non-transient) flux at 15.5 GHz is 0.24 mJy (J. Bright et al. 2017, in prep). To model the non-transient flux ($S_{\nu, \text{baseline}}$) at other frequencies (ν) we adopt a spectral index of -0.8 as follows:

$$S_{\nu, \text{baseline}} = 0.24 \left(\frac{\nu}{15.5 \text{ GHz}} \right)^{-0.8} \text{ mJy} \quad (1)$$

This spectrum is expected if the non-transient radio flux is due to a lobe that was created by the jet that was active prior to the disruption. Our model for the baseline flux (Eq. 1) is broadly consistent with both the 5 GHz flux that is resolved-out in the EVN observations (Romero-Cañizales et al. 2016) and the pre-TDF radio detection with FIRST (Becker et al. 1995).

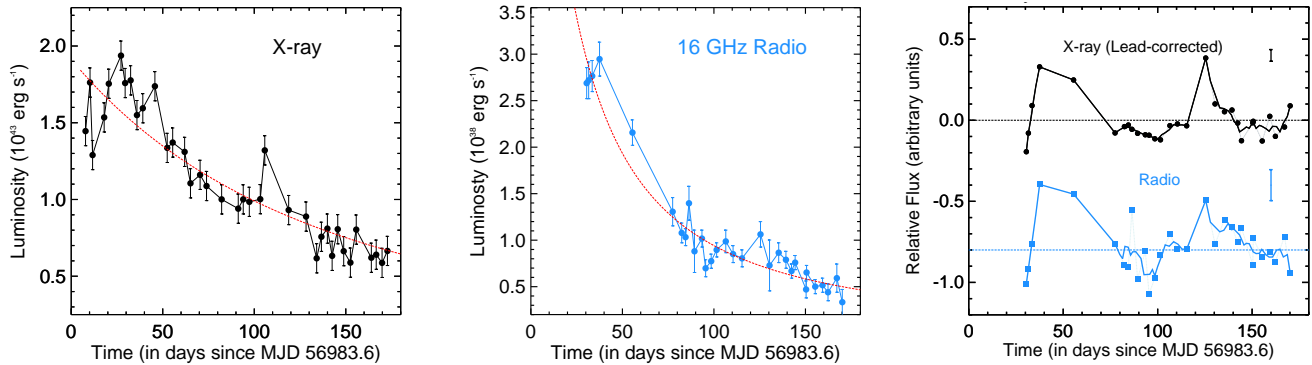


FIG. 1.— De-trending the light curves. *Left*: ASASSN-14li’s X-ray (0.3-1 keV) light curve (black data points) along with the best-fit power-law decay model (dashed red curve). *Center*: The 16 GHz transient radio light curve (blue data points) and its best-fit power-law decay model (dashed red curve). The error bars represent the 68% confidence interval (including the systematic uncertainty of converting from count rate to luminosity). A constant value of 0.24 mJy was subtracted from the observed 16 GHz light curve to exclude the non-transient component (see Sec.2.1). *Right*: The relative light curves obtained by subtracting the best-fit power-law decay. X-ray and the radio fractional variability amplitudes on top of the power-law decay are $10\pm 1\%$ and $16\pm 1\%$, respectively. The mean flux is shown by the dotted line. The solid curves are running averages over a 10 day window (except when the gap between observations in longer than 10 days), are shown to guide the eye. Typical 68% uncertainties are shown as vertical bars.

The AMI measurement of the baseline flux at 16 GHz is about 0.1 mJy higher than the value assumed by Alexander et al. (2016).

2.2. X-ray Data Reduction

ASASSN-14li was discovered on MJD 56983.6 (Holoien et al. 2016a). About a week later, *Swift* started monitoring the source with a mean observing cadence of one visit (1-3 ks) every three days. This cadence was maintained for about 270 days but the monitoring campaign suffered from longer data gaps thereafter because of sun angle constraints. AMI started monitoring ASASSN-14li at 16 GHz 31 days after its discovery (van Velzen et al. 2016b). The radio campaign lasted for roughly 140 days with an observing cadence of about one visit every four days. To ensure that the cross-correlation function (CCF) is not heavily biased by the X-ray data points, we only used the first 180 days of X-ray data for evaluating the CCF between the X-ray and the 16 GHz AMI data. All the radio data used here is as published by van Velzen et al. (2016) and Alexander et al. (2016). We re-analyzed the X-ray data to estimate the fluxes and discuss those details below.

We first extracted a cleaned eventlist from each XRT observation by running the `xrtpipeline ftool` on the raw level-1 XRT products. The data were all taken in the photon-counting (PC) mode, and because ASASSN-14li was bright, pile-up was present in each of the monitoring observations. To reduce the effect of pile-up we extracted source events—with patterns 0-12 in the energy range of 0.3-10.0 keV—from an annulus instead of a circular region as prescribed by *Swift*’s data analysis guide³. For each individual XRT monitoring observation we fit the X-ray point spread function (PSF) with a king model (Moretti et al. 2005) between $15''$ - $50''$ and then estimated the radius between $0''$ - $15''$ where the model diverges from the data. We set the inner exclusion radius for the annulus to be this divergence radius. In summary, instead of using a fixed inner radius for the annulus for all observations (Miller et al. 2015), we estimated it directly

from the data for each pointing. The background events were extracted from a concentric annulus with an inner and outer radii of $70''$ and $250''$, respectively. All the data reduction, *viz.*, extracting eventlists, images, spectra, etc, was done using the `HEASoft` version 6.18 (release 2016 February 8) and the most recent *Swift* calibration data base (CALDB) files were utilized.

The X-ray spectrum of ASASSN-14li is very soft with almost all counts between 0.3 and 1.0 keV, and is well-fit with a blackbody model (Miller et al. 2015). Therefore, we modeled its X-ray spectra with a blackbody function. The individual *Swift*/XRT monitoring observations lack the necessary signal-to-noise to constrain the blackbody temperature and radius. To be able to constrain the model parameters in each XRT observation, we carried out an analysis similar to the approach followed by Burrows et al. (2011). We grouped data from neighboring epochs until the total counts exceeded 3000 and summed spectra using the `ftool sumpha`. The corresponding response files, *i.e.*, the RMFs (Response Matrix Files) and the ARFs (Ancillary Response Files) were weighed as per ASASSN-14li’s counts in the individual epochs and combined using the tasks `addrmf` and `addarf`, respectively. This procedure translated to combining anywhere between 4-10 neighboring observations. We then fit these averaged X-ray spectra (0.3-1.0 keV) separately with a blackbody model defined as `phabs*zashift(phabs*bbbodyrad)` in XSPEC (Arnaud 1996). The best-fit model parameters are listed in Table 1. It is evident that the temperature changes were modest during the first 180 days. This is consistent with Fig. 3 of Miller et al. (2015) and more recently with Fig. 5 of Brown et al. (2017). To obtain the blackbody normalization in each epoch, we modeled the individual XRT spectra with the same blackbody model, but froze the disk temperature and the absorbing column to the values of the nearest averaged spectrum. The 0.3-1.0 keV fluxes estimated from this approach are listed in Table 3.

For each XRT pointing we also extracted a mean source count rate corrected for the background, the exposure and vignetting using the `ftool xrtlccorr`. PSF correction was also performed by setting the keyword `psfflag =`

³ <http://www.swift.ac.uk/analysis/xrt/pileup.php>

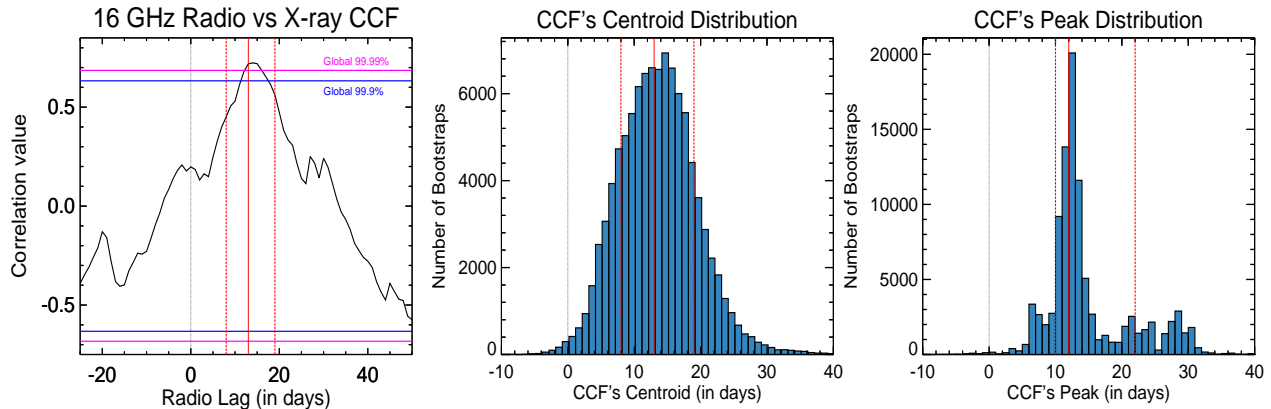


FIG. 2.— X-ray and radio cross-correlation. *Left-Panel:* X-ray vs 16 GHz radio Cross-Correlation Function (CCF) showing that the radio emission lags the X-ray radiation by 13_{-5}^{+6} days (see Sec. 3). The global 99.9% (blue) and the 99.99% (magenta) white noise statistical confidence contours for a search between -25 and 50 days are also shown. The significance contours were generated using Monte Carlo simulations (see Sec. 3.2). The centroid and the peak distributions of the CCF are shown in the middle and right panels, respectively. These show the uncertainty in the centroid and the peak of the X-ray–radio lag after taking into account both the measurement and the sampling uncertainties of the light curves. The red dashed vertical lines in these two panels indicate the $1\text{-}\sigma$ deviation away from the median values (solid red lines).

yes. Exposure maps were also extracted to account for bad pixels. The resulting source count rates are shown in Table 3.

3. TIMING/CROSS-CORRELATION ANALYSIS

We computed the interpolated cross-correlation function (ICCF; see Gaskell & Peterson 1987; White & Peterson 1994; Peterson et al. 2004 and the references therein) between the 16 GHz radio and the X-ray light curves. As explained in Sec. 2.1), we subtracted the non-transient emission at 16 GHz. But we stress that the observed correlation and the lag (below) are independent of the value of the baseline flux.

Welsh (1999) argued that long-term trends in the light curves can sometimes bias the ICCF analysis and thus de-trending with a smooth function can improve the ability to recover the correlation and the lag between the two time series under consideration. Therefore, we first de-trended both the X-ray and the radio light curves with a power-law decay model. The two light curves along with their best-fit decay model of the form $A \times (t - t_0)^{-\alpha}$ (where A , t_0 , and α are the model parameters, and t is the time in days) are shown in Figure 1 (left and middle panels). The ICCF was then computed between the residual light curves (data minus the best-fit model). We also experimented with other de-trending models, viz., a linear model, and a second order polynomial model. The ICCFs in all these cases showed clear evidence for a radio lag around 13 days. Because of the theoretical expectation that the bolometric TDF light curves should decay as a power-law (Rees 1988; Lodato et al. 2009), which is consistent with most X-ray observations (Komossa 2002), we adopted the analysis corresponding to the power-law decay model.

Similar to Maoz & Netzer (1989), we evaluated a two-way ICCF where we computed the cross-correlation twice, once by interpolating the radio light curve and then by interpolating the X-ray data. The final ICCF is an average of the two. The two-way ICCF will ensure that the cross correlation function is not biased towards either light curve (Maoz & Netzer 1989). The underly-

ing algorithm for evaluating the ICCF is as follows. We first displace one of the light curves by a certain time lag and linearly interpolate it onto the time values of the other light curve. Then we estimate a correlation value corresponding to that particular time lag. We build the entire ICCF by repeating this process for lags between -25 and 50 days in intervals of 1 day. The final ICCF is shown in the left panel of Fig. 2

3.1. Visually assessing the cross-correlation

To allow a visual assessment of the strength of the cross-correlation, we placed the X-ray and the radio light curves on top of each other (Fig. 1, right panel). We first displaced the observed X-ray light curve by 13 d, the median of the ICCF’s centroid (see Sec. 3.3). We then interpolated the X-ray light curve onto the time values of the radio data. The interpolated X-ray light curve (black) is overlaid on the 16 GHz radio data (blue) in the right panel of Fig. 1. It is clear that they both exhibit the same variability features. The solid curves are a running mean of the data points in a 10 day window.

3.2. Statistical Significance Contours

The X-ray–radio ICCF in Fig. 2 clearly shows a peak centered around 13 days⁴. To assess the statistical significance of this peak, we estimated the global 99.9% and 99.99% Gaussian white noise confidence contours as follows. First, we extracted M values from a Gaussian distribution with a mean of zero and a standard deviation equal to the standard deviation of the observed de-trended X-ray light curve. Here, M is the number of data points in the observed X-ray light curve. By assigning these M values to be the flux values at the times of the observed X-ray light curve, we constructed a synthetic de-trended X-ray light curve sampled exactly as the observed X-ray light curve. This synthetic X-ray light curve was then cross-correlated with the de-trended

⁴ The notation throughout the paper is such that a positive lag in the ICCF implies that the radio lags behind the X-rays.

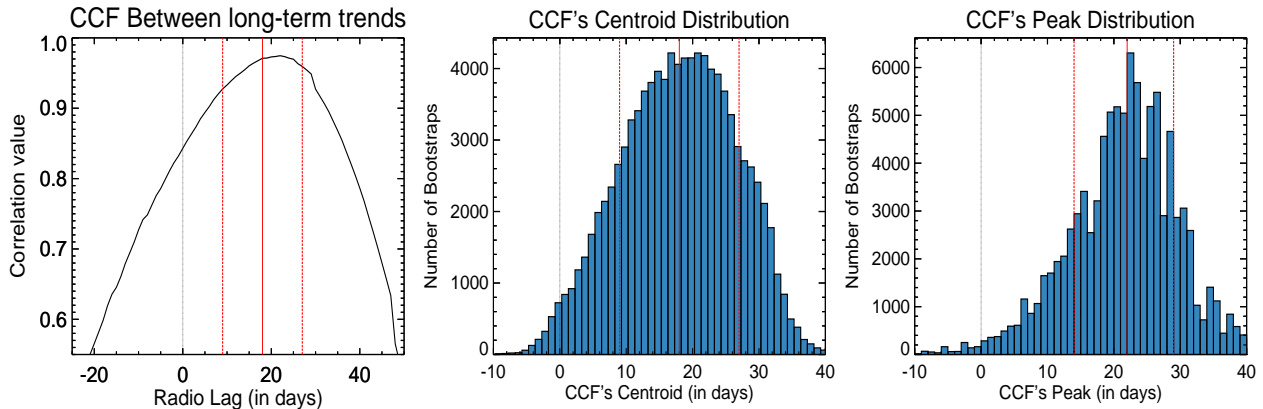


FIG. 3.— X-ray and Radio cross-correlation between the long-term trends. Same as Fig. 2 but here we compute the ICCF between the radio and the X-ray long-term trends indicated by the dashed red curves in the left and the middle panels of Fig. 2. The centroid of the lag is 18_{-9}^{+9} days and is consistent with the lag measurement from cross-correlation between the short-term radio and X-ray fluctuations shown in Fig. 2. The presence of lag between the long-term trends implies that the entire radio flux is regulated by the X-rays (see Sec. 4.3).

radio light curve exactly as the observed ICCF. This procedure was repeated 10^6 times to construct 10^6 synthetic CCFs. We then constructed a distribution of all CCF values between -25 and 50 days. From this distribution we extracted the global 99.9 and 99.99% significance levels (see the left panel of Fig. 2).

3.3. Uncertainty on the Lag's Centroid and Peak

We extracted the errorbars on the peak and the centroid lag values using the Flux Randomization (FR) and the Random Subset Selection (RSS) methods as described in Peterson (2004). These account for the measurement and the sampling uncertainties of both the light curves. We estimated the distribution of the centroid (middle panel of Fig. 2) and the peak (right panel of Fig. 2) of the ICCF. The centroid was estimated using all correlation values greater than 0.8 times the peak. Because these distributions need not be Gaussian (Peterson et al. 2004), we estimated the confidence intervals equivalent to the 1σ errorbars of a Gaussian, i.e., the upper limit corresponds to a lag value above which 15.87% of the realizations are present, while the lower limit on the peak/centroid lag corresponds to a lag below which 15.87% of the realizations lie. These are indicated as dashed vertical red lines in the middle and the right panels of Fig. 2.

Finally, we also repeated the entire cross-correlation analysis with the X-ray count rate light curve (instead of flux) and the resulting ICCF is consistent with the ICCF of the X-ray flux versus the radio flux. This is not surprising as the X-ray spectral changes were only modest (see Table 1) and therefore count rate serves as a good indicator of the flux.

3.4. Time Lag between the X-ray and Radio Trends

We also extracted an ICCF between the best-fit power-law trends of the X-ray and the 16 GHz radio light curves. These are indicated as red dashed curves in the left and middle panels of Fig. 1. Because the highest cross-correlation power in these trends is at the lowest frequency, one might expect the CCF of these two declining light curves to simply peak at zero lag. Instead, we find

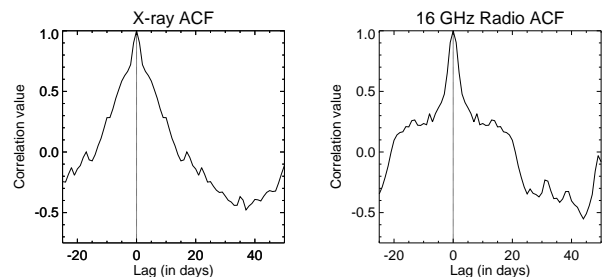


FIG. 4.— X-ray and radio auto-correlation functions (ACFs). The ACF of the X-ray and the radio light curves are shown in the left and the right panels, respectively. Both are obtained using the same CCF parameters as in Fig. 2. The difference in the two ACF shapes is only an artifact of the difference in the sampling of their respective light curves (see Sec. 3.5).

that the strongest cross-correlation value is at a finite lag (see Fig. 3). The best-fit lag value is 18_{-9}^{+9} days and is consistent with the lag obtained from only the short-time scale fluctuations of the light curves, i.e., the CCF of the de-trended light curves (Fig. 2). This strongly suggests that not just the variations in the radio and the X-rays are correlated but the entire radio-emitting region is regulated by the X-ray engine.

3.5. Auto-correlation Functions

A cross-correlation function is a convolution of the auto-correlation function (ACF) with the transfer function. A lag is real only if it originates from the transfer function and not from the ACF itself. To make sure that the lag seen in Fig. 2 does not originate from either of the X-ray or the radio ACF we evaluated both and show them in Fig. 4. Clearly, both the ACFs are centered on zero lag and thus assert that the observed lag originates from the transfer function.

The difference in the shapes of the two ACFs is due to the different sampling of the two light curves. Whether the X-ray light curve is lead-corrected and interpolated onto the radio epochs or vice versa: the resulting ACFs are similar (which is expected for two light curves that are highly correlated).

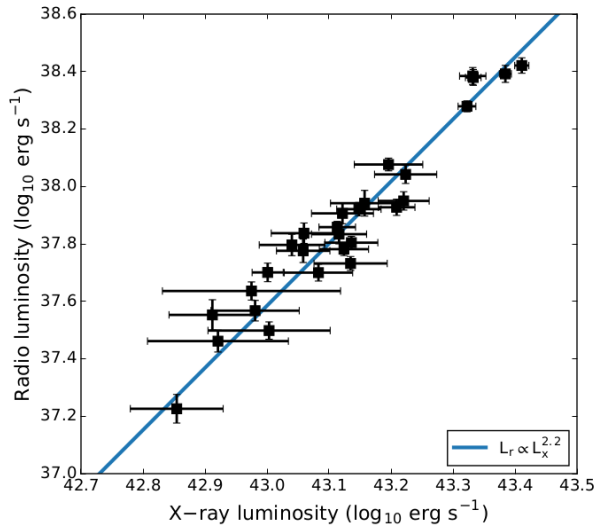


FIG. 5.— X-ray and radio luminosity. Here we show the lead-corrected X-ray luminosity and the 16 GHz radio luminosity (after subtracting the non-transient flux). The correlation between the luminosity in these two wavelengths can be described as $L_{\text{radio}} \propto L_{\text{X-ray}}^{2.2 \pm 0.2}$. The reduced χ^2 of the best-fit power-law relation is 0.96. This index suggests that ASASSN-14li’s accretion and jet power are linearly coupled (see Sec. 4.4).

3.6. Correlation between X-ray and Radio Luminosity

After correcting for the lag between the X-ray and the radio light curves, we compared the contemporaneous luminosities at these two frequencies. Since the X-ray data is sampled with a higher cadence, we interpolated the X-ray light curve onto the time stamps of the radio data. Following the “Nuker method” (Tremaine et al. 2002), we fit a power-law to the X-ray versus radio luminosity by minimizing the following merit function:

$$\chi^2(t_{\text{lag}}) = \sum \frac{(L_{\text{radio}}(t) + a - bL_{\text{X-ray}}(t + t_{\text{lag}}))^2}{\sigma_{\text{radio}}^2 + b^2\sigma_{\text{X-ray}}^2} \quad (2)$$

Here b is the X-ray–radio power-law index and a is the normalization; $L_{\text{X-ray}}(t)$ and $L_{\text{radio}}(t)$ denote the logarithm of the X-ray and the radio luminosity, respectively, as a function of time. $\sigma_{\text{X-ray}}$ and σ_{radio} are the logarithm of the X-ray and radio measurement uncertainties, respectively. The X-ray light curve is interpolated to a time $t + t_{\text{lag}}$, with t_{lag} being the observed CCF lag. Under the assumption that Eq. 2 follows χ^2 statistics (Tremaine et al. 2002), we can estimate the statistical uncertainty on the best-fit power-law index. To estimate the systematic uncertainty on the power-law index, we sampled the observed distribution of lags (Fig. 2, middle panel) and obtained a distribution of best-fit values of b .

We find the following best-fit power-law index $b = 2.16 \pm 0.10$ (statistical) ± 0.18 (systematic), with a reduced χ^2 of 0.96. The data and this power-law relation are shown in Fig. 5. If no lag is applied to the X-ray light curve, the scatter in the luminosity–luminosity relation is significantly larger and the reduced χ^2 of the best-fit power-law is 3.5. An interpretation of the X-ray–radio luminosity relation is presented in Sec. 4.4.

4. SPECTRAL/SYNCHROTRON ANALYSIS

4.1. Evolution of the Peak Frequency

Using the formulae of synchrotron emission and self-absorption (e.g., Pacholczyk 1970) and an electron energy (E_e) distribution that follows a power-law ($N_e dE_e \propto E_e^{-p} dE_e$), Marscher & Gear (1985) derived the dependence of the peak radio flux (S_{peak}) on the frequency at peak (ν_{peak}) for an adiabatically expanding region in a conical jet to be,

$$S_{\text{peak}} \propto \nu_{\text{peak}}^{\frac{10(p-1)}{7p+8}} \quad (3)$$

The above equation (Eq. 20, in Marscher & Gear 1985) assumes that the magnetic field strength (B) scales with the radius, r , (perpendicular to the jet axis) as $B \propto r^{-1}$ which is the case for a conical jet (Readhead et al. 1978; Falcke & Biermann 1995). Using an electron power-law index (p) between 2 and 3, the above equation then translates to

$$S_{\text{peak}} \propto \nu_{\text{peak}}^{0.57 \pm 0.12} \quad (4)$$

On the other hand, the peak synchrotron flux of a cloud that is expanding radially is given by Eq. 17b of van der Laan (1966):

$$S_{\text{peak}} \propto \nu_{\text{peak}}^{\frac{7p+3}{4p+6}}, \quad (5)$$

or, for $2 < p < 3$,

$$S_{\text{peak}} \propto \nu_{\text{peak}}^{1.27 \pm 0.06} \quad (6)$$

The difference in the two cases is due to the scaling of the magnetic field and the particle energy with radius. For an adiabatically expanding blob in a conical jet geometry, the energy of a relativistic electron (E) falls off with radius as $E \propto r^{-2/3}$ (see Marscher 1980). While for a cloud of electrons that is adiabatically expanding in a spherical geometry, we have $E \propto r^{-1}$ (see van der Laan 1966)⁵.

Eqs. 4 and 6 can be compared to the observed evolution of ASASSN-14li’s radio SED to discriminate between an expanding jet and an expanding spherical cloud. Alexander et al. (2016) modeled each radio SED with a single volume that is in equipartition. Using their values of the peak flux and frequency we find $S_{\text{peak}} \propto \nu_{\text{peak}}^{0.61 \pm 0.04}$.

In order to extract the peak flux and the frequency at peak in a model-independent way, we fit the radio SEDs with a simple bending power-law function of the form:

$$S_\nu = \frac{S_0 \nu^{-\alpha_1}}{1 + \left(\frac{\nu}{\nu_{\text{bend}}}\right)^{(\alpha_2 - \alpha_1)}} \quad (7)$$

Here, S_0 and ν_{bend} are the normalization and the frequency at which the SED turns over, respectively. α_1

⁵ The scaling of the particle energy with source radius can be derived from the ideal gas equation for relativistic particles as follows. The ideal gas equation of state for relativistic particles is $Pr \propto n_e^{4/3}$, where Pr and n_e are the pressure and the electron density in the gas, respectively. We have $Pr = n_e \langle E \rangle$, where $\langle E \rangle$ is the mean energy of an electron in the gas, hence $\langle E \rangle \propto n_e^{1/3}$. For a spherical cloud of relativistic electron gas, the electron density falls off with radius as $n_e \propto r^{-3}$. Thus $\langle E \rangle \propto r^{-1}$ for a spherical geometry. However, for an expanding jet, $n_e \propto r^{-2}$ and thus $\langle E \rangle \propto r^{-2/3}$.

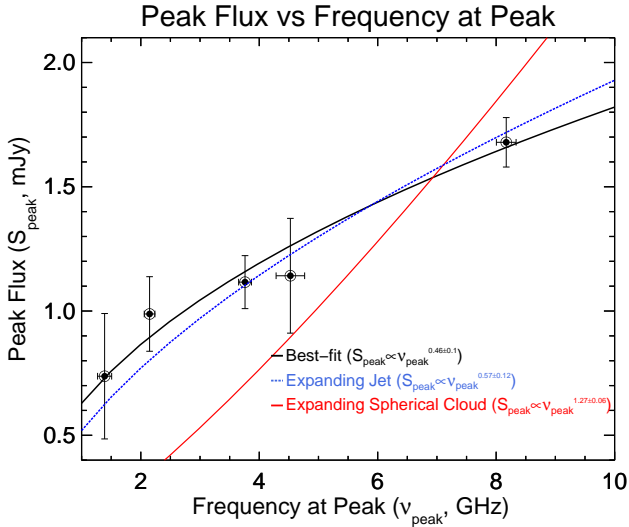


FIG. 6.— Radio SED evolution: Conical jet versus a spherical cloud. Evolution of the peak radio flux vs the frequency at peak (black data points). The best-fit power-law index of 0.46 ± 0.1 is shown by a solid black curve while the index for an adiabatically expanding jet (Marscher 1980) and an adiabatically expanding spherical cloud (van der Laan 1966) are shown by the dashed blue and the red curves, respectively.

and α_2 are the spectral index for frequencies (ν) much smaller than and much larger than ν_{bend} , respectively. We fixed the low-frequency slope (α_1) to be equal to the value for synchrotron self-absorption ($\alpha_1 = -2.5$). Using the five of the best sampled SEDs from Alexander et al. (2016), i.e., those taken on 2015 Jan 6/13, 2015 Mar 13, 2015 April 21/22, 2015 June 16/21 and 2015 Aug 28/Sept 8/11, we find that the observed peak flux ($S_{\text{peak,obs}}$) and the frequency at peak ($\nu_{\text{peak,obs}}$) evolve as

$$S_{\text{peak,obs}} \propto \nu_{\text{peak,obs}}^{0.46 \pm 0.1} \quad (8)$$

This observed scaling disfavors a uniformly expanding single spherical cloud model and is consistent with the bulk of the radio emission originating from a conical geometry that is adiabatically expanding, see Fig. 6.

4.2. Single-zone Models

Consider a spherical region of radius R that is uniformly filled with magnetic fields (B) and relativistic electrons with an energy distribution $N_e d\gamma_e = K \gamma_e^{-p} d\gamma_e$, where γ_e and K are the electron Lorentz factor and the normalization, respectively. When observed at a distance D , the observed synchrotron flux of this region is given by

$$S_\nu = \delta^2 \frac{R^2}{4D^2} \frac{\epsilon_{\nu'}}{\kappa_{\nu'}} (1 - e^{-\kappa_{\nu'} R}) \quad (9)$$

Here δ is the Doppler factor of the region, and ν is the observed frequency. The synchrotron absorption ($\kappa_{\nu'}$) and emission ($\epsilon_{\nu'}$) coefficients depend on the magnetic field, the electron energy distribution, and the frequency in the rest-frame of the jet, $\nu' = \nu/\delta$. We solve for the normalization of these coefficients by assuming equipartition between the energy in the electrons and the magnetic field, $B^2/8\pi = \int N_e d\gamma_e$. Equipartition implies a minimum in the total energy of the

system (i.e., the sum of the energy in the magnetic field and the synchrotron-emitting particles). Observations of the lobes of radio galaxies (Croston et al. 2005; Kataoka & Stawarz 2005; Harwood et al. 2016) as well as AGN jets (Burbidge 1956; Readhead et al. 1978; Herrnstein et al. 1997; Falcke et al. 1999) provide strong evidence that equipartition is commonly reached for these sources. We confirmed that for $\gamma_{\text{max}} \gg \gamma_{\text{min}}$, our implementation of the synchrotron formalism (Eq. 9) gives the same results as the fitting formula for synchrotron emission given in Chevalier (1998).

As expected based on earlier work (Alexander et al. 2016; Krolik et al. 2016), we find that the synchrotron emission from a single region (Eq. 9) provides a reasonable fit to the radio SEDs of ASASSN-14li. For this fit we adopted $\gamma_{\text{min}} = 1$, $p = 2.2$ and $\gamma_{\text{max}} = 10^4$, but we stress that the resulting magnetic field and radius are only weakly dependent on these assumptions. For $\delta = 1$ (i.e., a non-relativistic outflow), this single-zone synchrotron model yields $B \approx 0.1$ G and $r \approx 4 \times 10^{16}$ cm for the observations of April 2015. For this magnetic field, the synchrotron cooling time at 10 GHz is ~ 10 yr, which supports the assumption that $\gamma_{\text{max}} \gg \gamma_{\text{min}}$. For this single-zone model, we find that the equipartition magnetic field scales with source size as $B \propto R^{-1.2}$.

The hotspots or the forward shock of a jet or outflow can be modelled using a single-zone equipartition model. However, establishing the observed cross-correlation in a single-zone model proves to be very difficult. First of all, the light crossing time of this region grows from ≈ 10 days to ≈ 30 days during the period of the 16 GHz monitoring observations, thus exceeding the duration of the cross-correlation lag. A second problem of establishing an X-ray–radio correlation within a single region is the long synchrotron cooling time at 16 GHz (~ 10 yr). Over the course of the 16 GHz monitoring observations (≈ 180 days), the region cannot radiate the energy it has received and thus the relative amplitude of fluctuations in the radio light curve due to fluctuations in the X-ray light curve should decrease with time.

To summarize, while a single-zone equipartition model for ASASSN-14li can reproduce the observed radio SEDs, its size is likely to be too large to produce variability on a 10 day timescale. Moreover, due to the long synchrotron cooling time, the addition of new energy to has a negligible effect on the radio flux. This leads us to consider a freely expanding jet as the source of the observed radio emission.

4.3. Adiabatic Jet Model

A conical equipartition jet model is widely used to explain the properties of compact radio cores of AGN and X-ray binaries (Blandford & Königl 1979; Falcke & Biermann 1995; Falcke et al. 1995; Crumley et al. 2017). In this model, electron acceleration happens internal to the jet (e.g., via collimation shocks) and equipartition is established at each radius in the jet that lies beyond the nozzle where the jet is accelerated.

Summing the optically thin synchrotron emission in the model for AGN jet cores yields the characteristic flat spectrum, $S_\nu \propto \nu^0$. However, the peak of the radio SED of ASASSN-14li decreases with time, $S_{\text{peak}} \propto \nu_{\text{peak}}^{0.5} \propto$

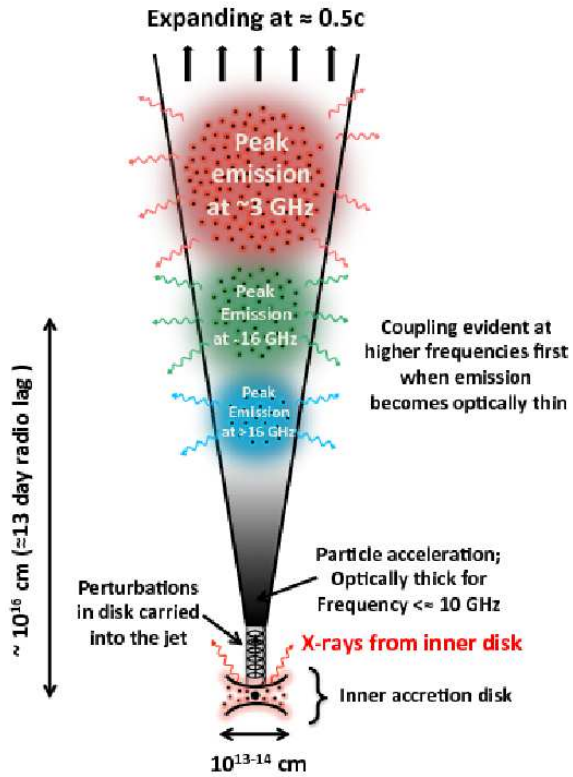


FIG. 7.— Schematic of the proposed jet model for the tidal disruption flare ASASSN-14li. Shown here is a snapshot of the jet at the end of the radio monitoring observations (June, 2015). The X-ray–radio correlation and the radio spectral evolution can both be explained as follows. First, perturbations in the accretion rate are manifested as X-ray flux variations and, via the disk–jet coupling, lead to perturbations in the jet power. The jet power is used to accelerate electrons, which produce synchrotron emission. As the synchrotron radiating electrons are swept further along the jet axis, they start to cool adiabatically. When their emission becomes optically thin to self-absorption at 16 GHz, at $\sim 10^{16}$ cm from the black hole (about 13 days later), the observed X-ray–radio correlation emerges. Applying our jet model to the radio observations of ASASSN-14li (Fig. 8), we estimate the jet flow velocity at these radii to be about $0.5c$.

$t^{-0.5}$. This suggests that we are observing the adiabatic evolution of electrons that have been heated prior to becoming optically thin to synchrotron self-absorption (Marscher & Gear 1985). Besides the evolution of the peak frequency (see Sec. 4.1), additional evidence for this adiabatic evolution is the apparent exponential turnover at $\nu \approx 15$ GHz in the radio SEDs (see Fig. 8). This turnover is most clearly seen in the radio data taken on 2015 Aug 28, Sep 8-11 (see Fig. 8). While this can be explained by synchrotron cooling, matching the cooling time at 16 GHz to the dynamical time requires a magnetic field that is two orders of magnitude higher than the observed equipartition value. In other words, the observed high-frequency break in the radio spectra can be explained by synchrotron cooling, but only if the particles were accelerated in a region with a magnetic field that is higher than the equipartition value. This can be established if the acceleration happened downstream in a jet (i.e., closer to the black hole), where the magnetic strength is larger. To include the effect of synchrotron cooling on the spectral shape, we allow the maximum Lorentz factor of the electrons, γ_{\max} , to be a free param-

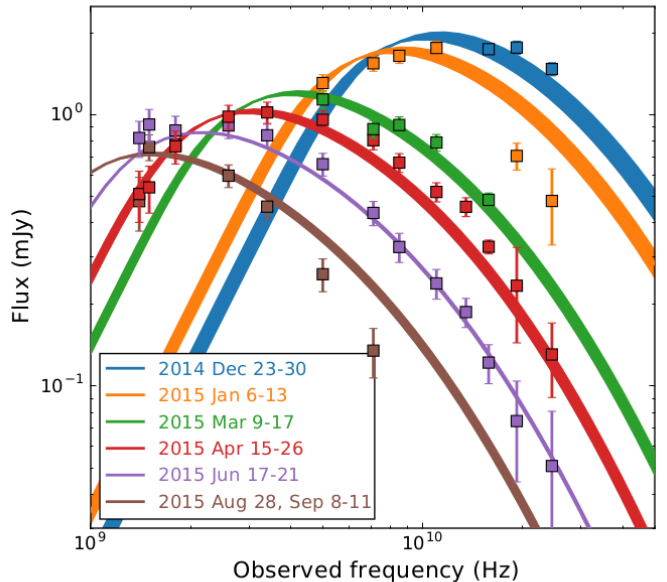


FIG. 8.— Adiabatic jet model and multi-frequency radio observations of ASASSN-14li. This jet model is a superposition of synchrotron emitting spheres, each expanding with the same velocity in a conical jet geometry. The electrons in each region in the jet cool adiabatically, which yields the decrease of the peak luminosity with time. Data points with the same colors are semi-simultaneous (epochs are labeled in the legend). The width of each model curve indicates the range of the predicted flux due to the temporal spread of the observations.

eter in our jet model.

To predict the light curve in an adiabatic jet model, we use a superposition of non-overlapping spheres in a conical geometry (Fig. 7), each with a flux given by their magnetic field and radius (Eq. 9). If each sphere receives the same amount of jet power, the total flux (i.e., the contribution from all the spheres) yields the well-known flat-spectrum, $S_\nu \propto \nu^0$. Following van der Laan (1966) and Marscher & Gear (1985) we account for adiabatic cooling of electrons via the normalization of the electron energy distribution

$$K(z > z_0) = (z/z_0)^{2(1-p)/3}. \quad (10)$$

Here z is distance measured along the jet axis and z_0 is the distance from the black hole where electrons are no longer accelerated and the jet starts to cool. Adding this cooling term to Eq. 9, we retrieve the scaling of Marscher & Gear (1985) for the peak flux with frequency at peak of an adiabatic jet (Eq. 3).

Since we have a rapid decrease in the accretion power, we expect that the jet power (Q_j) downstream from the jet head (z_{head}) will decrease. We model this with a power-law scaling,

$$Q_j(z, t) = (z/z_{\text{head}}(t))^{c_Q}, \quad (11)$$

with c_Q a free parameter. A second free parameter of our jet model is the scaling of the magnetic field along the jet axis

$$B(z, t) = B_0(z/z_0)^{c_B} \times Q_j^{1/2}(z, t). \quad (12)$$

If no magnetic energy is lost and the jet can freely expand to yield a conical geometry we expect $c_B =$

TABLE 2
BEST-FIT PARAMETERS OF AN ADIABATIC JET MODEL.

Relevant equation	Free parameters	$\phi = 1/5$	$\phi = 1/10$	$\phi = 1/15$ d
$B(z) = B_0(z/10^{15}\text{cm})^{c_B}$	B_0 (G)	9.6 (2.3)	7.6 (2.0)	8.0 (2.0)
	c_B	-1.02 (0.06)	-1.02 (0.05)	-1.07 (0.05)
$Q_{\text{jet}} \propto (z/z_{\text{head}})^{c_Q}$	c_Q	1.20 (0.4)	1.20 (0.4)	1.40 (0.2)
	$\log_{10} \gamma_{\text{max}}$	1.9 (0.4)	2.0 (0.3)	2.0 (0.2)
$z_{\text{jet}}(t) = v_{\text{jet}}(t - t_0)$	t_0 (MJD + 56887)	63 (11)	64 (11)	48 (12)
	v_{jet} (c)	0.37 (0.1)	0.62 (0.2)	0.71 (0.2)
Inferred parameters				
$\tau(16\text{ GHz}) = \kappa z_{16} = 1$	z_{16} ($\times 10^{16}$ cm)	$3.3^{+2.1}_{-2.0}$	$3.4^{+3.9}_{-1.6}$	$1.5^{+2.8}_{-1.2}$
$v_{\text{lag}} = (c \tau_{\text{lag}}/z_{16} + \cos i)^{-1/\gamma}$	v_{lag} (c)	$0.6^{+0.3}_{-0.2}$	$0.6^{+0.3}_{-0.2}$	$0.3^{+0.3}_{-0.2}$

NOTE. — The first six rows of the second column list the parameters of our jet model, with the relevant equations listed in the first column (see Sec. 4 for details). Their best-fit values (including 1σ uncertainties) are listed in the third to last columns, for three different values of the jet opening angle (ϕ). We can use the best-fit parameters to infer the radius where the jet becomes optically thin to self-absorption at 16 GHz (z_{16}). Using the observed lag between the radio and the x-ray light curves (τ_{lag}) we can compute the mean communication velocity (v_{lag}) between the black hole accretion disk and the 16 GHz self-absorption radius. We find that this estimate of the disk-jet communication velocity is consistent with the best-fit jet velocity (v_{jet}). All parameters listed here are estimated after adopting a jet inclination of $i = 60^\circ$.

–1 (Blandford & Rees 1974; Blandford & Königl 1979; Falcke & Biermann 1995). We stress that c_B and c_Q are not degenerate; c_B parameterizes how the radio flux from every regions in the jet changes as it expands while c_Q determines how the jet power scales relative to the peak jet power carried by the jet head.

The next two free parameters of our model concern the jet dynamics. Motivated by the inference that a linear growth provides a good description of the equipartition radius as a function of time in a single-zone synchrotron model (Alexander et al. 2016; Krolik et al. 2016), we assume a linear growth of jet head with time

$$z_{\text{head}}(t) = v_{\text{jet}} \delta(t - t_0) \quad , \quad (13)$$

with v_{jet} the rest-frame jet velocity and t is measured in the observer frame.

The last two free parameters in our model are the jet opening angle $\phi = r/z$ and the inclination, i . When the inclination is known, the Doppler factor can be computed using the jet velocity, $\delta = 1/(\gamma_{\text{jet}}(1 - \beta_{\text{jet}} \cos i))$. We also compute the emission from the counter jet, observed at $i - \pi$, but its contribution is sub-dominant for most inclinations.

Eqs. 9–13 together yield our jet model. This model has nine free parameters, (v_{jet} , t_0 , B_0 , z_0 , c_Q , c_B , γ_{max} , ϕ , and i), compared to the 82 observations of the radio flux (the combination of the WSRT, AMI, and VLA data). For comparison, determining the velocity in a single-zone equipartition model requires six parameters: v , t_0 , B_0 , i , γ_{max} , plus a factor to account for the geometry of the emitting region.

If no adiabatic cooling is included, z_0 is simply a normalization constant with no physical meaning, i.e., it can be set to any value. However, when cooling is included (Eq. 10), z_0 can be thought of as the distance from the black hole where adiabatic cooling becomes important. We set $z_0 = 10^{15}$ cm, but we stress that this choice has no effect on the inferred jet dynamics or magnetic field scaling along the jet axis. When adiabatic cooling starts,

the jet internal energy scales as $z^{-8/3}$ (Crumley et al. 2017), hence for our choice of z_0 the jet has lost ~ 10 of its energy by the time of the first radio observations. (In principle, z_0 can be constrained if we include a self-consistent treatment of synchrotron cooling in our jet model; while this is beyond the scope of this work, we do note that $z_0 \ll 10^{15}$ cm can be ruled-out since this yields a γ_{max} that is too low to explain the observed radio SEDs).

We fixed the jet inclination at its a priori most-likely value, $i = 60^\circ$, but we will explore less probable inclinations below. Finally, the opening angle of the jet is poorly constrained by the radio observations alone. To allow the new jet to be freely expanding, it likely has to remain within the volume swept clear by the jet that was active prior to the tidal disruption. We therefore adopt $\phi = 1/10$ as a fiducial value and also consider the best-fit jet parameters for larger/smaller opening angles.

In our fit for the parameter of the adiabatic jet model, we enforced a 5% minimum statistical uncertainty on the radio data. This avoids putting too much weight on the early VLA observations, where the statistical uncertainty almost certainly exceeds the variance due to the limitations of our simple model. To subtract the non-transient radio flux, we use Eq. 1. If we instead adopt the non-transient flux that was used in the analysis of Alexander et al. (2016), we infer similar values for the free parameters of our model.

We use a least-squares fit to estimate the parameters of our jet model; the results are summarized in Table 2. The reduced χ^2 of the best fit is 3.6. To approximately include the variance due to the limitations of our model into the derived parameters, we multiplied the statistical uncertainty of the best-fit parameters by $\sqrt{3.6}$.

We find that the inferred jet velocity depends on the assumed opening angle, for $1/15 < \phi < 1/5$ we obtain $0.3 < v_{\text{jet}}/c < 0.7$. The inferred values of the other parameters are essentially independent on the opening angle. Since the jet Lorentz factor is modest, the effect

on the jet inclination on the best-fit parameters is relatively small (e.g., for $\phi = 1/10$ and $i = 90^\circ$, $v_{\text{jet}} = 0.6c$, while the same jet opening angle observed at $i = 0$ yields $v_{\text{jet}} = 0.5c$). We find that 80% of the total jet flux is reached when the first four synchrotron-emitting spheres are summed, with the first sphere (i.e., the jet head) contributing about 30% of the total flux.

The power-law index that sets the scaling of the magnetic field strength along the jet axis is a free parameter in our model. We find $c_B = -1.02 \pm 0.03$, in excellent agreement with the expected $B \propto z^{-1}$ scaling for a conical jet geometry and conservation of magnetic energy (Blandford & Königl 1979; Falcke & Biermann 1995). By extrapolating to $z = 0$, we estimate that the jet was launched near the second week of June, 2014.

When the magnetic field is known, our jet model can be used to estimate the optical depth of each zone in the jet. Since an X-ray–radio cross-correlation can only be observed when the synchrotron emission is optically thin, the radius where $\tau = 1$ at 16 GHz provides a consistency check on our jet model. This radius yields an estimate of the communication velocity between the disk and the region from where the majority of the 16 GHz flux originates. The communication velocity can be estimated as $v_{\text{lag}}/c = \gamma^{-1}(\tau_{\text{lag}}c/z_{\text{lag}} + \cos(i))^{-1}$, with τ_{lag} the observed delay between the X-ray and the radio light curves. Using our best-fit value for the magnetic field at MJD=57018 (which corresponds to the peak of the first correlated feature in the two light curves, about one month into the 16 GHz monitoring campaign, see Fig. 1), this estimate of v_{lag} is consistent with jet velocity predicted by our model (see Table 2).

4.4. Coupling between Accretion Rate and Jet Power

Under the assumption of a constant expansion velocity, our estimate of the jet power scaling obtained in the previous subsection can be translated to a scaling of the jet power with time. Along the jet-axis, $Q_j \propto z^{1.2 \pm 0.4}$. Under the assumption of a constant expansion velocity, we thus obtain $Q_j \propto t^{-1.2 \pm 0.4}$. Interestingly, this relation is consistent with the slope of the observed X-ray flux decay, $L_{\text{X-ray}} \propto (t - t_0)^{-1.7 \pm 0.1}$ (here we fixed the time normalization, t_0 , to our estimate of the time when the jet was launched). This X-ray flux decay index is also close to the expected fallback rate of the stellar debris, $t^{-5/3}$ (Phinney 1989). Because the thermal X-ray energy spectrum suggests an efficient accretion disk we expect the X-ray luminosity, $L_{\text{X-ray}} \propto \dot{m}$ (mass accretion rate). We thus find evidence for a linear coupling between the accretion rate and jet power.

Because the entire radio flux is correlated with the X-rays (see Fig. 3) we can also use the observed correlation between the X-ray and the radio luminosities to estimate the coupling strength between the mass accretion rate and the jet power (see also J. Bright et al. in prep 2017).

Using eq. (7) of Heinz & Sunyaev (2003) it can be seen straightaway that the optically thin synchrotron emissivity, j_ν , at a given radio frequency (ν) for a power-law distribution of electrons with index p is given as,

$$j_\nu = J_p K B^{\frac{p+1}{2}} \nu^{-\frac{p-1}{2}} \quad (14)$$

where J_p is a constant weakly dependent on p , and B is the magnetic field strength, and K is defined as before

(see 4.2).

Thus, at a given radio frequency

$$j_\nu \propto L_{\text{radio}} \propto K B^{\frac{p+1}{2}} \quad (15)$$

where L_{radio} is the radio luminosity at ν . The jet power scales with the magnetic field strength as $Q_j \propto B^2$ and, under the assumption of equipartition $K \propto B^2$. Combining these two relations, we find (Heinz & Sunyaev 2003, their Eq. 16)

$$L_{\text{radio}} \propto Q_j^{1+\frac{p+1}{4}} \quad (16)$$

For, $2 < p < 3$ the index is 1.875 ± 0.125 .

From the observed X-ray and radio luminosities, we have $L_{\text{radio}} \propto L_{\text{X-ray}}^{2.2 \pm 0.2}$. Combining these into Eq. 16 results in

$$Q_j \propto \dot{m}^{1.2 \pm 0.1} \quad (17)$$

We thus see that the accretion and the jet power follow a roughly linear coupling. A caveat is that Eq. 16 is valid for a single region in the jet. While the 16 GHz emission is dominated by the radius where the jet becomes optically thin to self-absorption, which are coupled to an earlier or later time phase of the X-ray light curve, other regions also provide a sub-dominant contribution to the 16 GHz flux. Correcting for this requires a more complete jet model than the toy model used in this work.

5. DISCUSSION

Our main conclusions, in order, are:

1. We detected a correlation, significant at greater than the 99.99% level, between the soft X-ray and the 16 GHz radio variability of the thermal TDF ASASSN-14li. The radio emission lags the X-rays by about 13 days (Figs. 2 & 3).
2. The cross-correlation is inconsistent with external emission models (i.e., shocks driven into the circumnuclear medium) since in such models the radio emission is expected to evolve independently of the accretion rate or fallback rate.
3. We propose that the electrons responsible for the observed synchrotron emission are accelerated inside a jet which provides a natural vehicle to couple the radio-emitting region with the X-ray emitting region (Fig. 7).
4. Emission from a cloud of electrons that is adiabatically expanding in a conical geometry also provides a good match to the observed evolution of the radio SEDs (Figs. 6 & 8).
5. The observed scaling between the X-ray and the 16 GHz radio flux suggests that the accretion and the jet power are roughly linearly coupled (see Sec. 4.4).

Below we discuss a few implications of these conclusions. First, we compare ASASSN-14li to sources on the fundamental plane and then briefly remark on the implications for jet physics.

5.1. Comparison to AGN and X-ray Binary Jets

Black holes accreting at only a few percent of their Eddington limit are known to exhibit accretion–jet coupling (Merloni et al. 2003; Falcke et al. 2004; Gallo et al. 2003). For some supermassive black holes it has been possible to detect a time lag on the order of a few tens of days between the radio emission from the compact jet core and the hard X-ray (>2 keV) emission (Marscher et al. 2002; Bell et al. 2011; Chatterjee et al. 2011). These observations all point to a coupling between black hole jets and accretion disks.

Work by Merloni, Heinz, & di Matteo (2003) and Falcke, Körding, & Markoff (2004) has shown that for black holes in the “hard-state” (see Remillard & McClintock 2006 for a definition of this accretion state), the hard X-ray (2–10 keV) luminosity, the 5 GHz radio luminosity and the black hole mass are correlated, thus spanning a plane. This relation—the fundamental plane of black hole activity—extends all the way from stellar to supermassive black holes, ranging over roughly seven orders of magnitude in black hole mass (see Fig. 9).

To place ASASSN-14li on the fundamental plane of black hole activity, the 5 GHz radio luminosity was estimated at each 16 GHz epoch by interpolating the radio SEDs using our best-fit jet model. It is evident that the soft X-ray luminosity and the 5 GHz radio luminosity of ASASSN-14li fall very close to the fundamental plane. Allowing the mass to vary in between 10^5 to $10^7 M_\odot$ the sources does not move significantly away from the plane.

Our finding that the X-ray and radio properties of ASASSN-14li are consistent with the fundamental plane of black hole activity could be considered surprising. First of all, the slope of the X-ray–radio correlation of ASASSN-14li (2.2, Fig. 5) is much steeper than slope of the plane (0.6), at a fixed black hole mass. Furthermore, the X-ray emission from ASASSN-14li is thermal and soft (0.3–1 keV), thus likely originating from an radiatively efficient accretion flow, the X-ray luminosity of sources on the fundamental plane is dominated by non-thermal emission (in the 2–10 keV band). These hard X-rays presumably originate from an X-ray corona rather than a radiatively efficient accretion disk. It has been suggested that the X-ray corona can either be an inefficient inner accretion flow (Yuan & Cui 2005) or the base of the jet—among other possibilities (Markoff et al. 2005). In either scenario, the X-ray emission site for these black holes is physically different from ASASSN-14li. The close match to the fundamental plane could simply be a coincidence—although we note that the output of the powerful jetted TDF *Swift* J1644+57 is also consistent with the fundamental plane (Miller & Gültekin 2011).

5.2. A Jet Power Dichotomy?

A linear coupling between the jet power and accretion power is well-established for radio-loud quasars (Rawlings & Saunders 1991; Falcke et al. 1995; van Velzen et al. 2015). The hard X-ray light curve of the powerful jetted TDF *Swift* J1644+57 closely matches the power-law decay expected for the fallback rate of the stellar debris (Levan et al. 2016). Since the X-rays of this source almost certainly originate from the base of a relativistic jet (however see, Kara et al. 2016), these

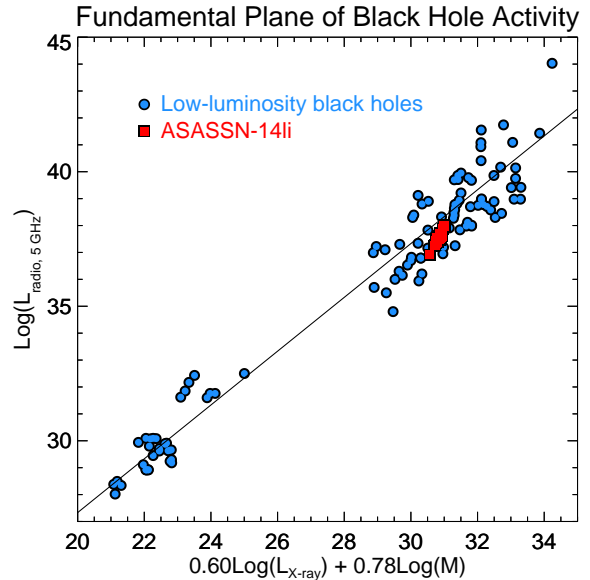


FIG. 9.— ASASSN-14li on the fundamental plane of black hole activity. The blue data show the fundamental plane of black hole activity as derived in Merloni et al. (2003) with their best-fit relation. Observations of ASASSN-14li data are shown in red (squares). $L_{X\text{-ray}}$, M , and $L_{\text{radio},5\text{GHz}}$ are the 2–10 keV X-ray luminosity, the black hole mass in units of solar mass, and the 5 GHz radio luminosity, respectively. Because ASASSN-14li is a very soft X-ray source (Miller et al. 2015), its X-ray luminosity is estimated in the 0.3–1.0 keV energy range.

observations suggest that *Swift* J1644+57 may also displays a linear disk–jet coupling. Combining this with our discovery of a linear coupling between the accretion rate and the jet power for ASASSN-14li, may lead one to conclude that a similar jet engine operates for both radio-loud quasars and jets from TDFs such as ASASSN-14li and *Swift* J1644+57. However this unified picture is challenged by the difference in radio luminosity between these two TDFs.

The difference in the jet energy of *Swift* J1644+57 and the equipartition energy of ASASSN-14li is about 4 orders of magnitude (Alexander et al. 2017). Relativistic Doppler boosting is not a solution to explain this difference since the late-time radio emission of *Swift* J1644+57 is most likely isotropic (Mimica et al. 2015). We further note that the host galaxies of these events have a similar central black hole mass, $M \sim 10^6 M_\odot$, as inferred from the host galaxy properties (Levan et al. 2016; Wevers et al. 2017). Since our jet model for ASASSN-14li requires adiabatic cooling to explain the evolution of the spectral energy distribution, the true jet energy of this source is likely to be an order of magnitude higher than the equipartition energy inferred from the radio SED (see Sec. 4.3). However, to be consistent with observed radio SED, the correction due to adiabatic cooling cannot be arbitrarily large. We thus conclude that the difference in isotropic jet power between *Swift* J1644+57 and ASASSN-14li is 2–3 orders of magnitude.

The difference in jet power could be explained by a difference in jet efficiency, i.e., the conversion of accretion power to jet power. Parameters that may affect this efficiency are black hole spin and the magnetic field near the horizon. Alternatively, to uphold a unified sce-

nario in which all TDFs have a similar jet efficiency, the amount of accretion energy available for jet production must be higher for *Swift* J1644+57. This difference could be established by the orbit of the star. Consider a deeply plunging orbit (i.e., a pericenter much smaller than the tidal radius). These events likely yield rapid circularization, and thus accretion, of the stellar debris (Dai et al. 2015). The result is a longer super-Eddington accretion phase compared to stars that are disrupted close to the tidal radius. If the jet is powered only when the accretion rate is super-Eddington (e.g., Coughlin & Begelman 2014), deeply plunging tidal disruptions could thus yield more powerful jets.

While a freely expanding jet appears to provide the only self-consistent explanation for both the observed radio SEDs and the X-ray–radio correlation of ASASSN-14li, an uncomfortable feature of this model is the requirement of a low external particle density on a scale of 10^{16} cm from the black hole. This can be reconciled if the newly launched TDF jet propagates along the same axis as the jet that was operating during the AGN activity prior to the stellar disruption. Thermal TDFs by black holes that had no active jet prior to the disruption may therefore not produce month-long radio flares. This

could explain the radio non-detection in a recent nearby TDF (Blagorodnova et al. 2017) where a radio flare similar to ASASSN-14li would have been detectable.

Acknowledgements: This work is based on observations made with *Swift*, a mission that is managed and controlled by NASA’s Goddard Space Flight Center (GSFC) in Greenbelt, Maryland, USA. The data used in the present article is publicly available through NASA’s *HEASARC* archive. We would like to thank Edo Berger, Bradley Cenko, Heino Falcke, Glennys Farrar, Rob Fender, Elmar K rding, Andrei Gruzinov, Jeroen Homan, Christian Knigge, Julian Krolik, Sara Markoff, Andrea Merloni, Giulia Milgori, James Miller-Jones, Gabriele Ponti, and especially Alan Marscher and Abdu Zoghbi for valuable discussions. Pasham is supported by NASA through an Einstein fellowship (PF6-170156) and van Velzen is supported by NASA through a Hubble Fellowship (HST-HF2-51350). All the data presented here is public and can be found in Table 3, van Velzen et al. (2016b), Alexander et al. (2016), and the NASA/*Swift* archive.

Facilities: AMI, VLA, Swift.

REFERENCES

- Alexander, K. D., Berger, E., Guillochon, J., Zauderer, B. A., & Williams, P. K. G. 2016, *ApJ*, 819, L25
- Alexander, K. D., Wieringa, M. H., Berger, E., Saxton, R. D., & Komossa, S. 2017, *ApJ*, 837, 153
- Arcavi, I., Gal-Yam, A., Sullivan, M., et al. 2014, *ApJ*, 793, 38
- Arnaud, K. A. 1996, in *Astronomical Society of the Pacific Conference Series*, Vol. 101, *Astronomical Data Analysis Software and Systems V*, ed. G. H. Jacoby & J. Barnes, 17
- Auchettl, K., Ramirez-Ruiz, E., & Guillochon, J. 2017, *ArXiv e-prints*, arXiv:1703.06141
- Bade, N., Komossa, S., & Dahlem, M. 1996, *A&A*, 309, L35
- Becker, R. H., White, R. L., & Helfand, D. J. 1995, *ApJ*, 450, 559
- Bell, M. E., Tzioumis, T., Uttley, P., et al. 2011, *MNRAS*, 411, 402
- Berger, E., Zauderer, A., Pooley, G. G., et al. 2012, *ApJ*, 748, 36
- Blagorodnova, N., Gezari, S., Hung, T., et al. 2017, *ArXiv:1703.00965*, arXiv:1703.00965
- Blandford, R. D., & Königl, A. 1979, *ApJ*, 232, 34
- Blandford, R. D., & Rees, M. J. 1974, *MNRAS*, 169, 395
- Bloom, J. S., Giannios, D., Metzger, B. D., et al. 2011, *Science*, 333, 203
- Bower, G. C., Metzger, B. D., Cenko, S. B., Silverman, J. M., & Bloom, J. S. 2013, *ApJ*, 763, 84
- Brown, G. C., Levan, A. J., Stanway, E. R., et al. 2015, *MNRAS*, 452, 4297
- Brown, J. S., Holoien, T. W.-S., Auchettl, K., et al. 2017, *MNRAS*, 466, 4904
- Burbidge, G. R. 1956, *ApJ*, 124, 416
- Burrows, D. N., Hill, J. E., Nousek, J. A., et al. 2005, *Space Sci. Rev.*, 120, 165
- Burrows, D. N., Kennea, J. A., Ghisellini, G., et al. 2011, *Nature*, 476, 421
- Cenko, S. B., Krimm, H. A., Horesh, A., et al. 2012, *ApJ*, 753, 77
- Chatterjee, R., Marscher, A. P., Jorstad, S. G., et al. 2011, *ApJ*, 734, 43
- Chevalier, R. A. 1998, *ApJ*, 499, 810
- Coughlin, E. R., & Begelman, M. C. 2014, *ApJ*, 781, 82
- Croston, J. H., Hardcastle, M. J., Harris, D. E., et al. 2005, *ApJ*, 626, 733
- Crumley, P., Ceccobello, C., Connors, R. M. T., & Cavecchi, Y. 2017, *ArXiv e-prints*, arXiv:1703.02842
- Dai, L., McKinney, J. C., & Miller, M. C. 2015, *ApJ*, 812, L39
- Esquej, P., Saxton, R. D., Komossa, S., et al. 2008, *A&A*, 489, 543
- Falcke, H., & Biermann, P. L. 1995, *A&A*, 293, 665
- Falcke, H., K rding, E., & Markoff, S. 2004, *A&A*, 414, 895
- Falcke, H., Malkan, M. A., & Biermann, P. L. 1995, *A&A*, 298, 375
- Falcke, H., Bower, G. C., Lobanov, A. P., et al. 1999, *ApJ*, 514, L17
- French, K. D., Arcavi, I., & Zabludoff, A. 2016, *ApJ*, 818, L21
- Gallo, E., Fender, R. P., & Pooley, G. G. 2003, *MNRAS*, 344, 60
- Gaskell, C. M., & Peterson, B. M. 1987, *ApJS*, 65, 1
- Gehrels, N., Chincarini, G., Giommi, P., et al. 2004, *ApJ*, 611, 1005
- Generozov, A., Mimica, P., Metzger, B. D., et al. 2017, *MNRAS*, 464, 2481
- Gezari, S., Heckman, T., Cenko, S. B., et al. 2009, *ApJ*, 698, 1367
- Giannios, D., & Metzger, B. D. 2011, *MNRAS*, 416, 2102
- Harwood, J. J., Croston, J. H., Intema, H. T., et al. 2016, *MNRAS*, 458, 4443
- Heinz, S., & Sunyaev, R. A. 2003, *MNRAS*, 343, L59
- Herrnstein, J. R., Moran, J. M., Greenhill, L. J., et al. 1997, *ApJ*, 475, L17
- Holoien, T. W.-S., Kochanek, C. S., Prieto, J. L., et al. 2016a, *MNRAS*, 455, 2918
- . 2016b, *MNRAS*, 455, 2918
- Irwin, J. A., Henriksen, R. N., Krause, M., et al. 2015, *ApJ*, 809, 172
- Kara, E., Miller, J. M., Reynolds, C., & Dai, L. 2016, *Nature*, 535, 388
- Kataoka, J., & Stawarz, L. 2005, *ApJ*, 622, 797
- Komossa, S. 2002, in *Reviews in Modern Astronomy*, Vol. 15, *Reviews in Modern Astronomy*, ed. R. E. Schielicke, 27
- Krolik, J., Piran, T., Svirski, G., & Cheng, R. M. 2016, *ApJ*, 827, 127
- Levan, A. J., Tanvir, N. R., Cenko, S. B., et al. 2011, *Science*, 333, 199
- Levan, A. J., Tanvir, N. R., Brown, G. C., et al. 2016, *ApJ*, 819, 51
- Lodato, G., King, A. R., & Pringle, J. E. 2009, *MNRAS*, 392, 332
- Maoz, D., & Netzer, H. 1989, *MNRAS*, 236, 21
- Markoff, S., Nowak, M. A., & Wilms, J. 2005, *ApJ*, 635, 1203
- Marscher, A. P. 1980, *ApJ*, 235, 386
- Marscher, A. P., & Gear, W. K. 1985, *ApJ*, 298, 114
- Marscher, A. P., Jorstad, S. G., G mez, J.-L., et al. 2002, *Nature*, 417, 625
- Merloni, A., Heinz, S., & di Matteo, T. 2003, *MNRAS*, 345, 1057
- Metzger, B. D., Giannios, D., & Mimica, P. 2012, *MNRAS*, 420, 3528
- Miller, J. M., & G ltekin, K. 2011, *ApJ*, 738, L13

- Miller, J. M., Kaastra, J. S., Miller, M. C., et al. 2015, *Nature*, 526, 542
- Mimica, P., Giannios, D., Metzger, B. D., & Aloy, M. A. 2015, *MNRAS*, 450
- Moretti, A., Campana, S., Mineo, T., et al. 2005, in *Proc. SPIE, Vol. 5898, UV, X-Ray, and Gamma-Ray Space Instrumentation for Astronomy XIV*, ed. O. H. W. Siegmund, 348–356
- Nakar, E., & Piran, T. 2011, *Nature*, 478, 82
- Pacholczyk, A. G. 1970, *Radio astrophysics. Nonthermal processes in galactic and extragalactic sources* (Freeman and Co., San Francisco)
- Pasham, D. R., Cenko, S. B., Sadowski, A., et al. 2017, *ApJ*, 837, L30
- Pasham, D. R., Cenko, S. B., Levan, A. J., et al. 2015, *ApJ*, 805, 68
- Perlman, E. S., Meyer, E. T., Wang, Q. D., et al. 2017, *ApJ*, 842, 126
- Peterson, B. M., Ferrarese, L., Gilbert, K. M., et al. 2004, *ApJ*, 613, 682
- Phinney, E. S. 1989, in *IAU Symposium, Vol. 136, The Center of the Galaxy*, ed. M. Morris, 543
- Piran, T. 2004, *Reviews of Modern Physics*, 76, 1143
- Prieto, J. L., Krühler, T., Anderson, J. P., et al. 2016, *ApJ*, 830, L32
- Rawlings, S., & Saunders, R. 1991, *Nature*, 349, 138
- Readhead, A. C. S., Cohen, M. H., Pearson, T. J., & Wilkinson, P. N. 1978, *Nature*, 276, 768
- Rees, M. J. 1988, *Nature*, 333, 523
- Remillard, R. A., & McClintock, J. E. 2006, *ARA&A*, 44, 49
- Romero-Cañizales, C., Prieto, J. L., Chen, X., et al. 2016, *ApJ*, 832, L10
- Saxton, R. D., Read, A. M., Komossa, S., et al. 2017, *A&A*, 598, A29
- Sądowski, A., & Narayan, R. 2016, *MNRAS*, 456, 3929
- Shappee, B. J., Prieto, J. L., Grupe, D., et al. 2014, *ApJ*, 788, 48
- Tchekhovskoy, A., Metzger, B. D., Giannios, D., & Kelley, L. Z. 2014, *MNRAS*, 437, 2744
- Tremaine, S., Gebhardt, K., Bender, R., et al. 2002, *ApJ*, 574, 740
- van der Laan, H. 1966, *Nature*, 211, 1131
- van Velzen, S., Falcke, H., & Körding, E. 2015, *MNRAS*, 446, 2985
- van Velzen, S., Frail, D. A., Körding, E., & Falcke, H. 2013, *A&A*, 552, A5
- van Velzen, S., Körding, E., & Falcke, H. 2011, *MNRAS*, 417, L51
- van Velzen, S., Mendez, A. J., Krolik, J. H., & Gorjian, V. 2016a, *ApJ*, 829, 19
- van Velzen, S., Farrar, G. R., Gezari, S., et al. 2011, *ApJ*, 741, 73
- van Velzen, S., Anderson, G. E., Stone, N. C., et al. 2016b, *Science*, 351, 62
- Wevers, T., van Velzen, S., Jonker, P. G., et al. 2017, *MNRAS*, 471, 1694
- White, R. J., & Peterson, B. M. 1994, *PASP*, 106, 879
- Yuan, F., & Cui, W. 2005, *ApJ*, 629, 408
- Zauderer, B. A., Berger, E., Soderberg, A. M., et al. 2011, *Nature*, 476, 425

APPENDIX

TABLE 3
X-RAY FLUX AND COUNT RATES.

ObsID ^a	MJD ^b	X-ray flux ^c	X-ray count rate ^d	χ^2/dof
00033539001	56991.423	1.494 ^{+0.069} _{-0.069}	0.333±0.009	1.08/15
00033539002	56993.878	1.821 ^{+0.039} _{-0.041}	0.465±0.009	1.90/25
00033539003	56995.271	1.332 ^{+0.090} _{-0.090}	0.292±0.011	1.11/8
00033539005	57001.597	1.586 ^{+0.094} _{-0.094}	0.396±0.013	1.45/10
00033539006	57004.128	1.813 ^{+0.098} _{-0.098}	0.406±0.013	0.64/12
00033539008	57010.794	2.002 ^{+0.096} _{-0.096}	0.508±0.014	1.29/15
00033539009	57013.057	1.817 ^{+0.038} _{-0.038}	0.431±0.008	1.42/25
00033539010	57016.052	1.836 ^{+0.072} _{-0.072}	0.427±0.010	1.25/22
00033539011	57019.507	1.601 ^{+0.093} _{-0.093}	0.409±0.013	1.79/11
00033539012	57022.708	1.648 ^{+0.076} _{-0.076}	0.389±0.010	0.88/16
00033539014	57029.313	1.796 ^{+0.029} _{-0.031}	0.422±0.007	1.66/31
00033539016	57036.042	1.381 ^{+0.082} _{-0.082}	0.373±0.013	1.68/9
00033539017	57039.029	1.417 ^{+0.024} _{-0.025}	0.372±0.007	1.01/29
00033539019	57045.552	1.354 ^{+0.029} _{-0.029}	0.353±0.007	1.00/27
00033539020	57048.750	1.142 ^{+0.097} _{-0.097}	0.279±0.012	1.20/5
00033539022	57054.003	1.199 ^{+0.071} _{-0.071}	0.279±0.010	0.86/10
00033539023	57057.520	1.124 ^{+0.042} _{-0.042}	0.278±0.006	1.06/23
00033539025	57065.776	1.034 ^{+0.052} _{-0.052}	0.256±0.007	0.70/14
00033539028	57074.842	0.972 ^{+0.036} _{-0.036}	0.237±0.005	0.96/23
00033539029	57077.569	1.034 ^{+0.078} _{-0.078}	0.234±0.010	1.21/6
00033539030	57080.888	1.018 ^{+0.066} _{-0.066}	0.226±0.008	0.56/8
00033539032	57086.878	1.035 ^{+0.041} _{-0.041}	0.264±0.006	0.69/22
00033539033	57089.340	1.364 ^{+0.078} _{-0.078}	0.314±0.010	0.78/11
00033539035	57102.389	0.962 ^{+0.043} _{-0.043}	0.246±0.006	0.86/18
00033539038	57111.895	0.918 ^{+0.038} _{-0.038}	0.235±0.006	0.51/19
00033539040	57117.683	0.637 ^{+0.077} _{-0.077}	0.146±0.010	0.03/2
00033539041	57120.278	0.782 ^{+0.038} _{-0.038}	0.188±0.005	0.97/14
00033539042	57123.540	0.837 ^{+0.088} _{-0.088}	0.172±0.010	0.78/3
00033539043	57126.134	0.654 ^{+0.073} _{-0.073}	0.146±0.009	1.68/3
00033539045	57129.198	0.833 ^{+0.054} _{-0.054}	0.180±0.007	0.90/8
00033539046	57132.457	0.685 ^{+0.049} _{-0.049}	0.159±0.007	0.29/7
00033539047	57136.116	0.608 ^{+0.044} _{-0.044}	0.146±0.006	1.58/7
00033539048	57139.309	0.831 ^{+0.045} _{-0.045}	0.185±0.006	0.92/11
00033539049	57147.558	0.641 ^{+0.037} _{-0.037}	0.132±0.004	1.00/10
00033539050	57150.218	0.662 ^{+0.032} _{-0.032}	0.152±0.004	1.00/15
00033539051	57153.414	0.607 ^{+0.031} _{-0.031}	0.140±0.004	1.93/13
00033539052	57156.349	0.687 ^{+0.042} _{-0.042}	0.144±0.005	1.04/9
00033539053	57173.036	0.611 ^{+0.066} _{-0.066}	0.127±0.008	0.97/3
00033539054	57176.097	0.585 ^{+0.041} _{-0.041}	0.131±0.005	1.18/7
00033539055	57179.029	0.551 ^{+0.065} _{-0.065}	0.118±0.008	0.03/2
00033539056	57182.094	0.425 ^{+0.046} _{-0.046}	0.101±0.006	0.32/3
00033539059	57191.806	0.541 ^{+0.033} _{-0.033}	0.128±0.004	0.40/9
00033539060	57194.660	0.548 ^{+0.032} _{-0.032}	0.127±0.004	0.96/10
00033539061	57200.375	0.524 ^{+0.042} _{-0.042}	0.119±0.005	0.48/6
00033539062	57203.767	0.441 ^{+0.032} _{-0.032}	0.107±0.004	1.99/8
00033539063	57226.248	0.413 ^{+0.031} _{-0.031}	0.091±0.004	0.69/6
00033539064	57230.374	0.442 ^{+0.047} _{-0.047}	0.103±0.006	1.23/3
00033539065	57236.361	0.387 ^{+0.032} _{-0.032}	0.090±0.004	1.35/5
00033539066	57238.820	0.408 ^{+0.026} _{-0.026}	0.105±0.004	1.89/9
00033539067	57242.081	0.417 ^{+0.026} _{-0.026}	0.102±0.004	1.36/9
00033539068	57246.867	0.339 ^{+0.025} _{-0.025}	0.082±0.003	0.76/6
00033539072	57357.325	0.276 ^{+0.021} _{-0.021}	0.061±0.003	0.41/6
00033539073	57360.180	0.347 ^{+0.029} _{-0.029}	0.076±0.004	1.15/5
00033539074	57363.911	0.395 ^{+0.026} _{-0.026}	0.089±0.003	1.08/8

TABLE 3 — *Continued*

ObsID ^a	MJD ^b	X-ray flux ^c	X-ray count rate ^d	χ^2/dof
00033539075	57366.897	$0.380^{+0.029}_{-0.029}$	0.078 ± 0.003	1.49/6
00033539078	57375.538	$0.442^{+0.041}_{-0.041}$	0.087 ± 0.005	0.76/4
00033539079	57378.075	$0.386^{+0.033}_{-0.033}$	0.077 ± 0.004	0.69/5
00033539082	57411.445	$0.336^{+0.030}_{-0.030}$	0.069 ± 0.004	0.30/4
00033539084	57417.485	$0.367^{+0.032}_{-0.032}$	0.078 ± 0.004	1.19/5
00033539087	57427.720	$0.293^{+0.033}_{-0.033}$	0.052 ± 0.003	0.23/2
00033539090	57435.706	$0.268^{+0.027}_{-0.027}$	0.049 ± 0.003	0.37/3
00033539091	57519.777	$0.195^{+0.024}_{-0.024}$	0.037 ± 0.002	1.02/2

NOTE. — ^a*Swift*-assigned observation IDs. ^bModified Julian Date. ^cThe X-ray fluxes were estimated from 0.3–1.0 keV bandpass and are in the units of 10^{-11} erg s⁻¹ cm⁻². The uncertainties indicate both the lower and the upper 1σ confidence levels. ^dThe X-ray count rates were also estimated from 0.3–1.0 keV bandpass and are in the units of counts per second. The reduced χ^2 along with the dof are indicated in the last column.